NANO LETTERS

Letter

pubs.acs.org/NanoLett

Plasmon-Enhanced Terahertz Photodetection in Graphene

Xinghan Cai,[†] Andrei B. Sushkov,[†] Mohammad M. Jadidi,[‡] Luke O. Nyakiti,[⊥] Rachael L. Myers-Ward,[¶] D. Kurt Gaskill,[¶] Thomas E. Murphy,[‡] Michael S. Fuhrer,[†,§] and H. Dennis Drew*[,†]

[†]Center for Nanophysics and Advanced Materials, University of Maryland, College Park, Maryland 20742-4111, United States

[‡]Institute for Research in Electronics and Applied Physics, University of Maryland, College Park, Maryland 20742, United States

[§]School of Physics, Monash University, Victoria 3800, Australia

[⊥]Texas A&M University, Galveston, Texas 77553, United States

[¶]U.S. Naval Research Laboratory, Washington, D.C. 20375, United States

Supporting Information

ABSTRACT: We report a large area terahertz detector utilizing a tunable plasmonic resonance in subwavelength graphene microribbons on SiC(0001) to increase the absorption efficiency. By tailoring the orientation of the graphene ribbons with respect to an array of subwavelength bimetallic electrodes, we achieve a condition in which the plasmonic mode can be efficiently excited by an incident wave polarized perpendicular to the electrode array, while the resulting photothermal voltage can be observed between the outermost electrodes.

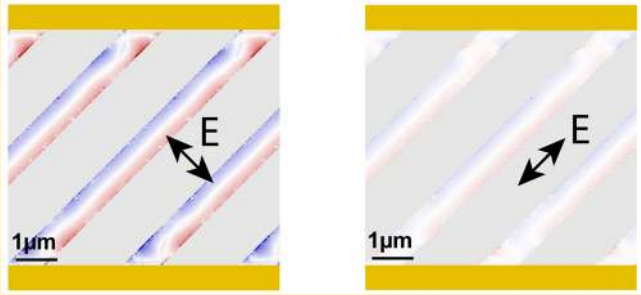

KEYWORDS: *Graphene, plasmons, terahertz, photodetection*

Graphene has unique optoelectronic properties[1−3] that result in a variety of potential photonic applications such as optical modulators,[4] plasmonic devices,[5−8] and THz emitters.[9] Particularly promising is terahertz (THz) photodetection, in which graphene devices may offer significant advantages over existing technology in terms of speed and sensitivity.[10−12] Because of graphene's small electronic heat capacity and relatively large electron−electron relaxation rate compared to its electron−phonon relaxation rate,[13,14] hot electron effects are important in graphene even at room temperature and have been exploited to realize fast, sensitive THz detection via the photothermoelectric effect[10,15,16] and bolometric effect.[17,18] However, a significant challenge remains in increasing graphene's absorption. Graphene's interband absorption is a frequency-independent constant $\pi\alpha \approx 2.3\%$ where α is the fine structure constant.[19,20] Owing to its zero band gap nature, doped graphene shows a relatively high DC conductivity, which results in a considerable Drude absorption (free carrier response) in the THz range.[21,22] However, the Drude absorption in graphene is strongly frequency dependent, decreasing as $(\omega\tau)^{-2}$ at high frequencies $\omega \gg 1/\tau$ where τ is the scattering time, proportional to graphene's mobility and typically 10−100 fs in graphene. Thus, the Drude absorption rolls off at lower frequencies in higher mobility (higher τ) graphene samples.

A number of efforts have been made to increase the absorption in graphene photodetectors. Quantum dots deposited on graphene can enhance the light-matter interaction;[23] however, the approach is likely limited to the visible or near-infrared where the interband absorption of the quantum dot lies, and the response times are slow. Locating the detector in a microcavity, which resonates at selected frequency, can enhance absorption, but to date this has been demonstrated only at near-infrared wavelengths[24] and would be cumbersome for long wavelength THz radiation. Coupling the detector to an antenna is a viable approach for frequencies up to the low THz, but there are few demonstrations of antenna-coupled graphene devices,[25] and the approach is applicable only to devices whose size is much smaller than the wavelength. In contrast to these approaches, plasmon resonances in finite-width graphene can provide a strong absorption that has a fast response (set by the thermal relaxation time[10]), is tunable over a broad range of frequencies in the THz through changing either the confinement size or the carrier density,[26,27] and is more amenable to fabrication of arrays for large-area detectors compared to antenna-coupled devices.

Here we demonstrate a room temperature THz detector based on large area arrays of epitaxial graphene microribbons contacted by metal electrodes, whose responsivity is significantly improved by the plasmon enhanced absorption. We show that if the opposing edges of the microribbons are directly contacted by metal electrodes, the altered boundary conditions at the graphene−metal interface and associated currents in the metal[28,29] make it difficult to directly excite plasmon

Received: January 13, 2015
Revised: March 18, 2015
Published: April 14, 2015

DOI: 10.1021/acs.nanolett.5b00137
Nano Lett. 2015, 15, 4295−4302

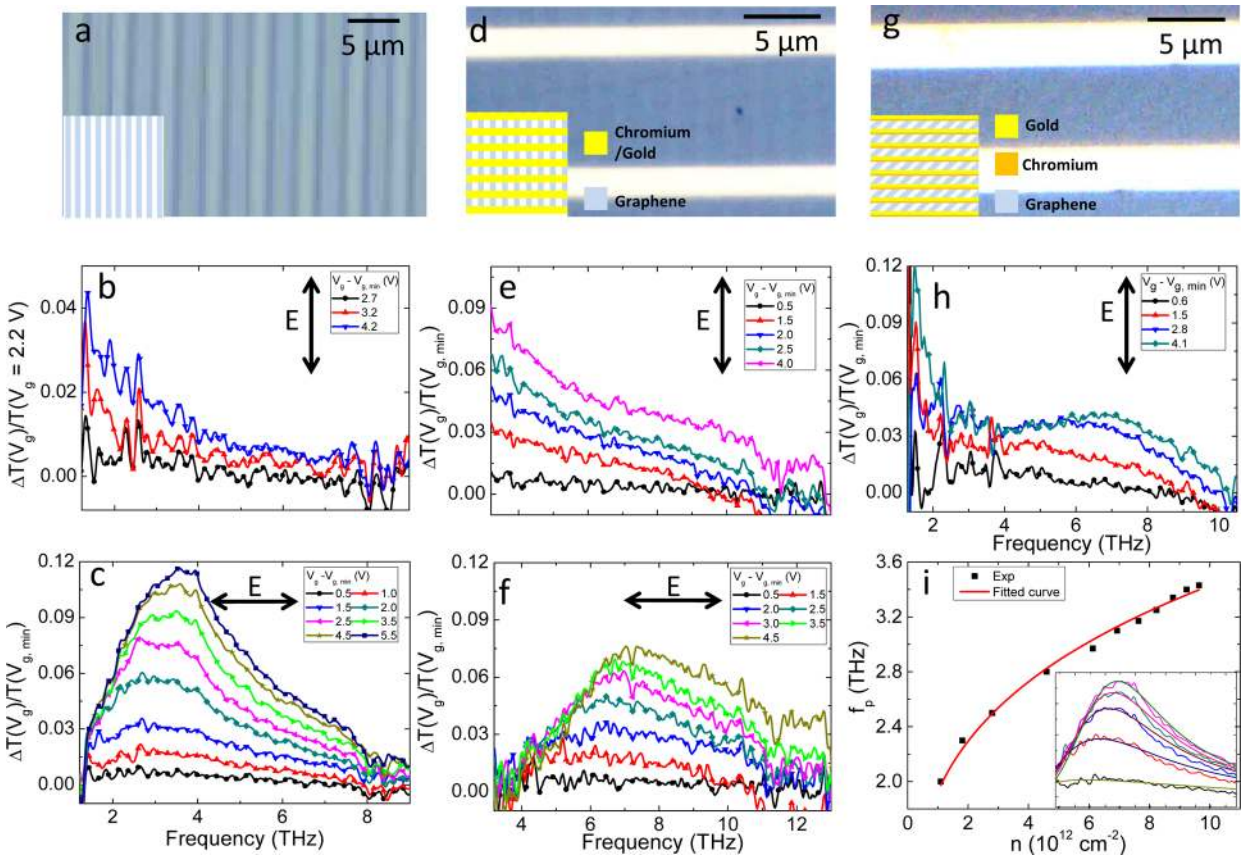

Figure 1. Attenuation spectra for (a–c) a graphene ribbon array with no metal electrodes, (d–f) a graphene ribbon array oriented orthogonal to a metal electrode grating, and (g, h) a graphene ribbon array tilted 45° with respect to a metal electrode grating. Optical micrographs of the devices are shown in panels a, d, and g. The insets show the corresponding schematics, respectively. Attenuation spectra at different gate voltages V_g are shown in panels b, c, e, f, and h. In panels c, e, f, and h, spectra are normalized by the spectrum at $V_g = V_{g,min}$, and in panel b at $V_g = V_{g,min} + 2.2$ V. The incident electric field is polarized parallel to the graphene ribbons in panels b and e and perpendicular to the graphene ribbons in panels c and f. In panel h, the incident electric field polarization is at 45° to the graphene ribbons and perpendicular to the metal grating. (i) Plasmonic resonance frequency f_p as a function of carrier density n for the device shown in panels a–c. Black points are extracted from fits of the data in panel c as described in text. Fits to data in panel c are shown as solid lines in inset. Red line: fit to eq 3 in text.

resonances. In contrast, if the ribbons are oriented perpendicular to the metal electrodes, then the subwavelength metal electrode pattern reflects the incident wave with the necessary polarization perpendicular to the ribbons and parallel to the electrodes, greatly reducing the plasmonic excitation.

We therefore adopt a novel geometry of graphene microribbons tilted at an angle with respect to the electrode array, in which the plasmon mode associated with currents transverse to the ribbon can be efficiently excited by light polarized perpendicular to the metal electrodes. By using dissimilar metal electrodes, we form a photothermoelectric detector from our tilted graphene microribbon array. We observe an enhanced photovoltage at room temperature when the carrier density of graphene is tuned such that the plasmon resonance frequency matches the THz continuous-wave excitation. The frequency and polarization-angle dependent absorption and the gate voltage and polarization-angle dependent photoresponse are well described by a simple plasmonic conductivity model for graphene.

Plasmon resonances in graphene have been previously studied in exfoliated graphene samples by using infrared nanoimaging[6,30] and by Fourier transform infrared spectroscopy (FTIR) in arrays of microribbons or disks patterned from large-area chemical vapor deposition-grown graphene.[7,31] The plasmon dispersion relation for graphene[7,26,27] is given by

$$q = \frac{\hbar(\varepsilon_1 + \varepsilon_2)}{4\pi^{1/2} e^2 v_F n^{1/2}} \omega(\omega + i/\tau) \tag{1}$$

where $\varepsilon_{1,2}$ is the dielectric constant of the media above/below graphene, n is the charge carrier density in graphene, $v_F = 10^6$ m/s is graphene's Fermi velocity, $\hbar$ is Planck's constant, and e is the elementary charge. We expect that a graphene ribbon of width W will determine the plasmon wavevector q such that

$$q = \frac{N\pi - \delta}{W} \tag{2}$$

where N is the harmonic order of the plasmonic mode, and δ is a phase shift upon reflection at the graphene edge. Numerical results indicate that $\delta = \pi/4$ for termination by dielectric.[32,33] Then we have for the plasmon resonance frequency

$$\omega_p = \left(\frac{3\pi^{3/2} v_F e^2}{\hbar(\varepsilon_1 + \varepsilon_2)}\right)^{1/2} \frac{n^{1/4}}{W^{1/2}} \tag{3}$$

For graphene on SiC ($\varepsilon_1 \sim 9.6$) with PEO electrolyte top gate ($\varepsilon_2 \sim 3$), the plasmon frequency $f_p = \omega_p/2\pi = 2.73$ THz $\times [n\ (10^{12}\ \mathrm{cm}^{-2})]^{1/4} \times [W\ (\mu\mathrm{m})]^{-1/2}$.

Here we show the first observation of such standing wave plasmons in monolayer epitaxial graphene on SiC (0001) substrates. We patterned large area graphene on SiC substrate

DOI: 10.1021/acs.nanolett.5b00137
Nano Lett. 2015, 15, 4295–4302

into a microribbon arrays using standard electron beam lithography (see Methods). Figure 1, panel a shows the optical micrograph of the sample with patterned electron-beam resist on top, which is used as a mask to etch graphene underneath (the graphene on SiC is not easily visible in optical microscopy). The total array size is 2 mm × 2 mm, the ribbon width is 2.3 μm, and the period of the array is 4.6 μm. The response of the device to THz excitation is characterized by FTIR (see Methods). The attenuation spectra with the excitation polarized parallel and perpendicular to the ribbon are plotted in Figure 1, panels b and c, respectively. In our experiment, the attenuation A is defined as $A = 1 - (T(V_g)/T(V_{g,min})) = \Delta T/T(V_{g,min})$, where $T(V_g)$ is the transmission when the applied gate voltage is V_g, and $T(V_{g,min})$ is the transmission at the charge neutral point. The carrier density in graphene is tuned by applying the gate voltage V_g through an electrolyte top gate [$LiClO_4$ + PEO (poly(ethylene oxide))]. Note that the spectra are normalized to the transmission at $V_{g,min}$ in Figure 1, panel c and to the transmission at $V_g = V_{g,min}$ + 2.2 V in Figure 1, panel b. Here, we take the spectrum which corresponds to the lowest carrier density of graphene achieved in each data set as the reference spectrum for normalization. As shown in Figure 1, panel b, a Drude response is observed, where the attenuation decreases monotonically with the frequency. A completely different line shape is seen for the attenuation spectra in Figure 1, panel c, when the incident light is polarized perpendicular to the ribbons, where we see enhanced absorption associated with excitation of the intrinsic plasmon.

In this device, where the ribbon width is fixed, a blue shift of f_p is observed when increasing n by raising the gate voltage. We modeled the spectra shown in Figure 1, panel c using a simple plasmonic conductivity model, with f_p and n as fit parameters and assuming a constant μ = 1300 $cm^2\ V^{-1}\ s^{-1}$ (see Methods). We then plot the modeled f_p versus n with a fit to eq 3, which gives $f_p = 1.92\ THz \times [n\ (10^{12}\ cm^{-2})]^{1/4}$. The prefactor 1.92 is very close to the expected value of 1.80 found from eq 3 with W = 2.3 μm. The inset of Figure 1, panel (i) shows the individual fits to selected curves from Figure 1, panel c.

To be used as a photodetector, graphene elements need to be connected via a conductive material to form a closed electrical circuit. Additionally, we expect that detectors exploiting hot electron effects will require electrode spacings comparable to the diffusion length of electrons due to electron−phonon scattering, expected to be less than 1 μm, far smaller than the THz wavelength in free space (~100 μm).[34]

Figure 1, panel d shows a graphene microribbon array, similar to that in Figure 1, panel a that is contacted by a perpendicular array of metal electrodes. The vertical graphene ribbons, faintly visible in Figure 1, panel d, are 0.6 μm wide with a period of 2 μm. The horizontal chromium/gold (4 nm/45 nm) electrodes were patterned on top of the graphene ribbons with an electrode width 1.7 μm and period of 9 μm. Figure 1, panels e and f show the measured attenuation spectra for two polarization cases. When the incident THz signal is polarized parallel to the microribbons, a Drude-like response is shown in Figure 1, panel e similar to Figure 1, panel b. For polarization perpendicular to the ribbons, a plasmon resonance is observed in Figure 1, panel f similar to Figure 1, panel c. Because the ribbons are about four-times narrower, the resonant frequency is higher by a factor of about two. Additionally, by comparing Figure 1, panels c and f, we find that the strength of the plasmon resonance is reduced in the metal-contacted case and is smaller than the strength of the resonance for the uncontacted ribbons. This is a consequence of the subwavelength metal grating that is a good reflector for radiation polarized parallel to the grating wires. The extinction coefficient of metal wire gratings scales in proportion to $(d/\lambda)^2$ at long wavelengths. This is a significant disadvantage of this scheme, since we expect that detectors will require even smaller electrode spacings on the micron scale is limited by the diffusion length.

To overcome the difficulties above, we adopt a design with graphene ribbons tilted at an angle with respect to the metal grating, as shown in Figure 1, panel g. In this device, the period of the graphene ribbon array is 2 μm, and the ribbon width is 0.6 μm, similar to the device in Figure 1, panels d−f. Bimetal electrodes (20 nm chromium + 25 nm gold) are deposited on graphene ribbons using a two-step shadow evaporation technique (see Methods). The graphene ribbons were inclined at an angle of θ = 45° with respect to the metal contacts and have a length of 5.7 μm, which is less than the previous device but still reasonably long, to allow some transmission of both polarizations as will be discussed in the next section. Light polarized perpendicular to the metal grid (which does not suffer from the polarizer effect) now has an electric field component perpendicular to the graphene ribbon axis and can therefore excite the transverse plasmon resonance. In this case, when the incident THz radiation is polarized perpendicular to the metallic grating, we can see evidence of gate-tunable plasmonic absorption in the attenuation spectrum, as shown in Figure 1, panel h. This is in contrast to Figure 1, panel e, where no plasmonic resonance can be seen for light polarized perpendicular to the metal electrode grating.

We further explore the polarization dependence of the tilted-ribbon array. Figure 2, panel a shows a color map of the polarization-dependent attenuation of the tilted ribbon array as described in Figure 1, panels g−h at $V_g = V_{g,min}$ + 5.4 V, which

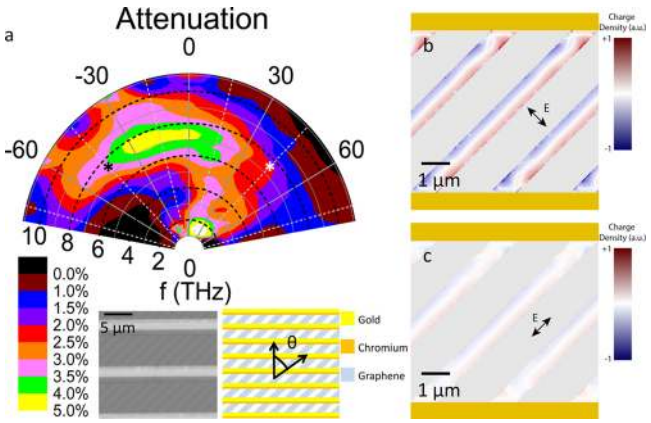

Figure 2. (a) Attenuation at $V_g = V_{g,min}$ + 5.4 V as a function of the frequency (radial axis) and the incident polarization (azimuthal axis). Inset: A scanning electron micrograph of a similar device (left) and the schematic of the device with the defined polarized angle θ of the incident light (right). The graphene ribbons are tilted 45° to the metal electrodes. (b, c) Simulated charge density profile in the graphene−metal microstructure at the plasmon resonance frequency. The polarization of the incident plane-wave (7.4 THz) is perpendicular to the graphene ribbons in panel b and parallel in panel c, corresponding to the points marked with black and white ∗ symbols in panel a, respectively. The same color scale is used for both panels.

DOI: 10.1021/acs.nanolett.5b00137
Nano Lett. 2015, 15, 4295−4302

is the highest gate voltage (highest carrier density) we achieved. The color scale indicates the normalized attenuation. Considering the metal polarizer effect, the attenuation here is defined as $A = (1 - T_{high}/T_{low}) \times f(\omega, \theta)$, where T_{high} is the transmission at $V_g = V_{g,min} + 5.4$ V, T_{low} is the transmission at $V_g = V_{g,min}$, and $f(\omega, \theta)$ is the experimentally determined extinction factor of the metal grating (see Methods for detailed information). Here, the attenuation is plotted as a function of frequency (plotted along the radial direction) and polarization angle, as defined in the inset schematic. The left inset of Figure 2, panel a shows an scanning electron microscopy (SEM) image of a similar device fabricated in the same way. Because the attenuation is multiplied by $f(\omega, \theta)$, the effect of the metal grating is included, and the polarization dependence is due to both the attenuation caused by graphene and metal grid. Additionally, the metal grid is symmetric with respect to polarizations at positive and negative angles $\pm\theta$, so asymmetry for $\pm\theta$ is caused by the tilting of graphene with respect to the metal grid. Indeed, we observe a highly asymmetric pattern of attenuation. When the angle of polarization is inclined in the direction parallel to the graphene ribbons ($\theta > 0$), we observe a Drude-like absorption spectrum, which decreases monotonically with frequency. By contrast, when the angle of polarization is inclined in the direction perpendicular to the ribbons ($\theta < 0$), we observe a peak in attenuation at ~7.4 THz, which we identify as the plasmon resonance frequency for these ribbons at this gate voltage. Figure 2, panels b and c show the simulated charge density oscillations in our device structure at this frequency for two polarization angles $\theta = \pm 45°$ (perpendicular and parallel to the ribbons, marked with black and white $*$ in Figure 2a), respectively (see Methods and the Supplementary Movie of the Supporting Information for detailed information). Compared to Figure 2, panel c, which shows a very weak charge density oscillation, Figure 2, panel b clearly displays a charge density wave excited by the incident electric field polarized perpendicular to the ribbons, which supports the identification of the observed attenuation peak at 7.4 THz and $\theta < 0$ as the transverse plasmon in our graphene–metal microstructure.

We next discuss a similar device but with a smaller electrode spacing more compatible with enhanced photothermoelectric detection. The device is fabricated using the same technique as the device shown in Figure 2, but here the graphene ribbon width is 1.1 μm, and the interelectrode spacing is 3.8 μm, which is closer to the estimated graphene hot carrier diffusion length to enhance the hot electron photothermoelectric effect and thus improve the detection efficiency. Ideally, an even shorter spacing could be adopted to make the device more dominated by diffusive cooling and put more light sensitive elements in series to enhance the photovoltage signal. The two-step shadow evaporation technique for asymmetric metal electrodes deposition is used so that each graphene channel (light sensitive part of the detector) has asymmetrical contacts (gold contact on the bottom edge and chromium contact on the top edge), which helps to generate a net photothermoelectric signal when the device is uniformly illuminated (see Methods). Figure 3 shows the attenuation spectra at different gate voltages for the incident light polarized with three typical angles. At $\theta = 60°$ (Figure 3a), because of the polarizing effect of the metal grid, which reduces the parallel component of the electric field, the effective electric field interacting with graphene is nearly parallel to the ribbons, which results in a dominant Drude response. At $\theta = -60°$ (Figure 3c), the effective electric field is close to perpendicular to the graphene ribbons, which excites the

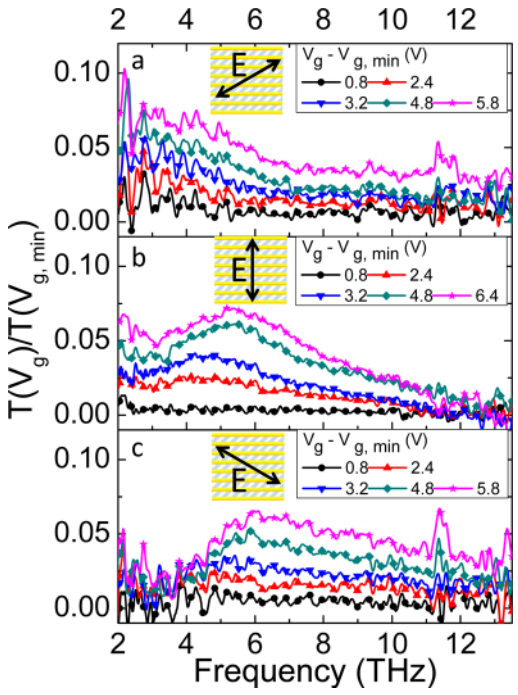

Figure 3. Attenuation at different V_g normalized by the spectrum at $V_{g,min}$ as a function of frequency for a device with graphene ribbon width of 1.1 μm and interelectrode spacing of 3.8 μm. (a) The incident polarization angle $\theta = 60°$, corresponding to a Drude response, (b) $\theta = 0°$, corresponding to a combined Drude and plasmon response, and (c) $\theta = -60°$, corresponding to a plasmon response. The insets show schematics of the device and the polarization of the incident light for each measurement, respectively.

transverse plasmons in the graphene ribbon, leading to increased attenuation at the plasmon resonant frequency, which is in the range 4–6 THz. As expected, the plasmon frequency increases with charge carrier density, which is varied by applying a gate voltage. Interestingly, at $\theta = 0°$ (Figure 3b), the angle at which the incident light is minimally absorbed by the metal grid, a combined response is observed, especially at high gate voltage. Here the components of the electric field parallel and perpendicular to graphene ribbons are nearly equal. At the highest gate voltage (magenta curve), the attenuation shows a local plasmonic peak at $f \approx 5.3$ THz and also a Drude response at low frequency.

Now we study the frequency and the polarization angle dependence of the attenuation at large positive gate voltage in more detail. Figure 4, panel a shows the attenuation of the same device studied in Figure 3 at $V_g = V_{g,min} + 6.5$ V, the highest gate voltage (carrier density) achieved. Similar to Figure 2, panel a, the color scale indicates the normalized attenuation. As shown in Figure 4, panel a, the attenuation peaks near $\theta = 0°$ because the metal grating reflects a large portion of the incident light polarized in other directions owing to the small spacing between metal electrodes. There is a local maximum at the frequency of ~5.3 THz corresponding to plasmon-enhanced attenuation, which is clearly separated from the Drude response at $f < 3$ THz. The plasmon peak is asymmetric in polarization angle with more weight at negative angle, while the Drude response occurs at positive angle.

To understand the relationship between plasmonic excitation and polarization, we developed a simple plasmon conductivity model to predict the expected absorption in the graphene

DOI: 10.1021/acs.nanolett.5b00137
Nano Lett. 2015, 15, 4295–4302

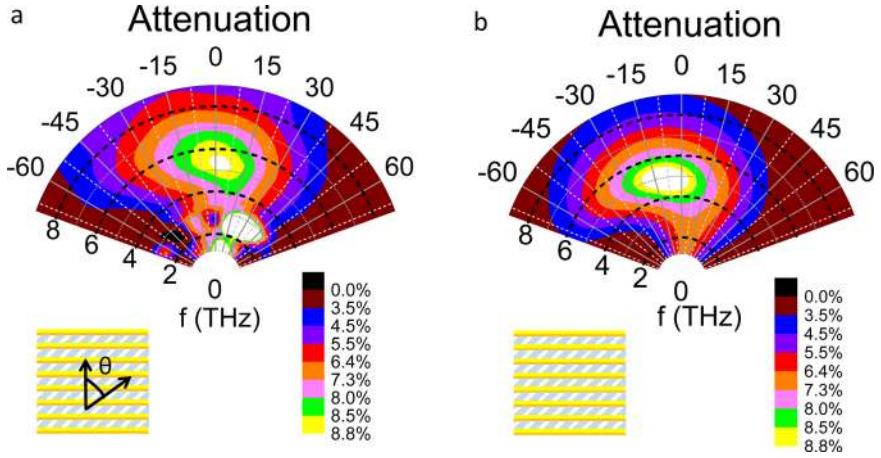

Figure 4. (a) Experimental attenuation at $V_g = V_{g,min} + 6.5$ V as a function of frequency (radial axis) and the incident polarization (azimuthal axis) for the same device of Figure 3. (b) Simulated attenuation of the device shown in panel a using the model discussed in the text. The insets show schematics of the devices and define the polarization angle θ.

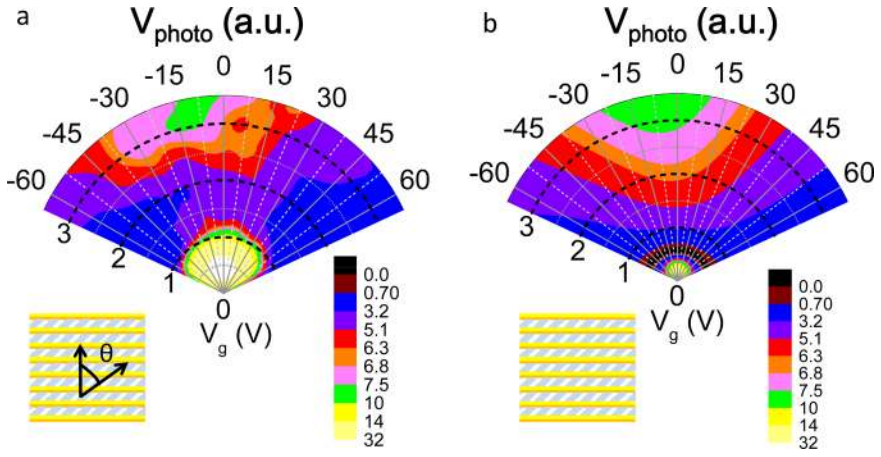

Figure 5. (a) Measured magnitude of the photovoltage for a tilted graphene ribbon array photodetector as a function of V_g (radial axis) and the incident polarization (azimuthal axis). The device is the same as in Figure 4, panel a, and the frequency of the laser excitation is 5.3 THz (175 cm^{-1}). (b) Simulated photoresponse of the same device using the model discussed in the text. The insets show schematics of the devices and define the polarization angle θ.

ribbons (see Methods). The modeled attenuation is plotted in Figure 4, panel b in the same way as the experimental data shown in Figure 4, panel a. The only free parameters of the model are the carrier density $n = 1.6 \times 10^{13}$ cm^{-2} and the mobility of graphene $\mu = 800$ cm^2 V^{-1} s^{-1}, which determines $\tau = 37$ fs. According to the model, the resistivity of the device at this gate voltage is ~500 Ω, which is lower than the measured resistivity of 1.4 KΩ. We attribute this difference to the contact resistance contribution in the two-probe transport measurement across multiple graphene/metal junctions. The model reproduces the features of the experimental data. A stronger attenuation peak at finite frequency is both predicted and observed when the angle of polarization is inclined toward the direction perpendicular to the graphene ribbons, which signifies the excitation of a transverse plasmonic resonance.

Next we discuss the electrical response to THz radiation of the same device as in Figures 3 and 4. Photoresponse measurements were performed using a continuous wave THz laser at 5.3 THz as the source (see Methods). Figure 5, panel a shows the photovoltage as a function of the applied top gate voltage (radial axis, measured relative to the charge neutral point) and the polarization angle of the CW excitation (azimuth). As shown previously,[10] the photovoltage is generated by the photothermoelectric effect[35−37] in graphene due to asymmetry of the electrodes. As reported in ref 10, this type of asymmetry leads to photothermoelectric voltage that is peaked near the Dirac point and monotonically decreases with the carrier density. Figure 5, panel b shows the modeled photoresponse as a function of gate voltage and polarization angle using the same parameters as in Figure 4, panel b, and a photothermoelectric model[10] with asymmetry generated by both an extra contact resistance $R_c = 35$ Ω at the gold electrode and the difference of the work function between chromium and gold (see Methods). Both the experimental and modeled signals show maxima at small gate voltages where the photothermoelectric responsivity peaks.[38−40] In addition, when the gate voltage is low, the photovoltage is symmetric around $\theta = 0°$ as the plasmon is only weakly excited in the low doped region. The signal for this device with a small metal spacing depends primarily on the polarizer effect of the metal electrodes and thus peaks with angle near $\theta = 0°$. At larger gate voltages, the photoresponse increases with increasing gate voltage. This rise is not due to increased responsivity, as observed earlier,[10] and explained within the asymmetric metal

DOI: 10.1021/acs.nanolett.5b00137
Nano Lett. 2015, 15, 4295−4302

electrodes model the responsivity decreases monotonically with increasing gate voltage at high gate voltage. Instead, the increase is explained by enhanced absorption in the device, which is due to (1) increase in DC conductivity with increased gate voltage and (2) resonant plasmonic absorption. The shift of the peak in photoresponse with respect to angle to $\theta < 0°$ clearly indicates that the plasmonic effect is dominant in increasing the absorption, similar to Figure 4, panels a and b.

To summarize, we have demonstrated a scheme for efficient THz excitation of resonant plasmons in graphene mircoribbon arrays contacted by metal electrodes with spacing much smaller than the free space wavelength. Resonant plasmon absorption enhances the absorption of radiation by graphene and therefore increases the external efficiency of graphene photothermoelectric detectors. Additionally the plasmon resonance is tunable through both geometry (ribbon width) and carrier density, enabling spectral resolution and tunability in graphene photothermoelectric detectors. In the device demonstrated here, the spectral resolution quality factor $Q = \omega_p\tau = 1.2$, is imited by the fairly low mobility of epitaxial graphene. Hence, for the present device, the THz attenuation is comparable in magnitude for the Drude and plasmonic absorption, as seen in, for example, Figure 3. However, our scheme has significant advantages if the mobility of the graphene can be increased, increasing scattering time τ, which determines the width of both the Drude response and plasmon resonance, achieving a high quality factor $Q = \omega_p\tau$ and large separation between Drude and plasmon responses. In addition, since the DC conductivity of graphene is $\sigma = ne\mu$, high mobility graphene would enable a strong plasmon resonance peak (which is proportional to the DC conductivity of the graphene sheet) at low doping where the thermoelectric response is maximized. Single-element graphene photothermoelectric detectors based on Drude absorption[10] have already shown an unprecedented combination of responsivity, NEP, and speed in few THz detection, and our scheme provides a route forward, as higher mobility is achieved in higher quality graphene, to detectors with higher efficiency (due to higher plasmonic absorption) and better spectral sensitivity (due to narrower plasmon resonance).

Methods. The starting material is epitaxial single-layer graphene on (0001) semi-insulating (resistivity $>10^9$ Ω-cm) 6H-SiC; see ref 41 for additional details. The 2D graphene is patterned into a ribbon array using electron beam lithography with 400 nm thick PMMA [poly(methy methacrylate), Micro Chem Corp.] resist as an etch mask and oxygen plasma treatment to remove exposed graphene. Chromium/gold electrodes (thickness 4 nm/45 nm) are thermally evaporated for the devices shown in Figure 1. For the bimetallic photothermal detectors, the liftoff mask is patterned via e-beam lithography using a bilayer resist [methyl methacrylate (8.5%)/methacrylic acid copolymer (MMA), Micro Chem Corp.; and PMMA]. Dissimilar metal contacts are fabricated in one lithographic step using a tilted-angle shadow evaporation technique[42] for the devices shown in Figures 2−5. Chromium (20 nm) and gold (25 nm) are deposited at different evaporation angles. As a final step, a droplet of electrolyte ($LiClO_4$/PEO = 0.12:1) is used to cover the whole device for applying top gate voltages.

Far infrared transmission measurements are performed in a BOMEM DA-8 FTIR system with mercury lamp as a source and 4 K silicon composite bolometer as a detector. The 2 × 2 mm^2 device is mounted on a copper plate with a 2 mm diameter aperture. The mounted sample is placed in vacuum at room temperature and is uniformly illuminated by the incident beam of 8 mm in diameter. We strongly overfill the sample aperture to minimize spectrometer diffraction losses at low frequencies. An electronically controlled rotating wire grid polarizer is placed in front of the sample. To minimize time drift of the signal, we consecutively measure transmitted spectrum through the device and an identical bare aperture placed in the sample position at each gate value, and their ratio gives us the absolute transmission. Finally, we divide all transmission spectra by the transmission spectrum measured at the Dirac point. Model calculations mimic this experimental procedure.

The THz photoresponse is characterized by illuminating the device with a chopped continuous wave laser beam and detecting the open-circuit photovoltage signal using a voltage preamplifier and lock-in amplifier. The THz laser is optically pumped by CO_2-laser resonator with Methanol-D (CH_3OD) vapors generating a line at 5.3 THz (175 cm^{-1}) frequency. The sample is mounted on the same copper plate as in the FTIR measurements, and the beam illuminates the device through the SiC substrate to avoid the absorption by the electrolyte. The same rotating polarizer is placed in front of the focusing parabolic mirror ($D = F = 50$ mm). The photovoltage is continuously normalized by the signal of the pyroelectric reference detector. The sample is mounted on an x-y-z scanning stage together with another pyro-detector, which is used for the power calibration (including signal for rotating polarizer).

The charge density oscillation at plasmon resonance frequency was obtained using a finite element method frequency-domain simulation. Plane-wave excitation (7.4 THz) was simulated with a polarization parallel and perpendicular to graphene ribbons. The geometrical parameters of the element are the same as the real device described in the text. The carrier density of graphene was taken to be 2×10^{13} cm^{-2}. The mobility was taken to be 5000 $cm^2\ V^{-1}\ s^{-1}$, which is possibly higher than that of the real device, to illustrate the plasmon mode more clearly.

To model the relative attenuation through the device at different gate voltages, we first calculate the transmission of the graphene ribbons using the thin-film expression:[43] $T = ((4n_1n_2)/(|n_1 + n_2 + Z_0\sigma|^2))$, where $n_1 = 1.73$ and $n_2 = 3.1$ are the refractive indices of the electrolyte and SiC substrate, $Z_0 = 377\ \Omega$ is the impedance of free space, and σ is AC conductivity of graphene. The AC conductivity σ can be written as $\sigma_d = \sigma_0/(1 + i\omega\tau)$ for Drude response and $\sigma_p = \sigma_0/(1 + i(\omega^2 - \omega_p^2)\tau/\omega)$ for plasmon excitation, where σ_0 is the DC conductivity, ω is the frequency, τ is the electron scattering time, and ω_p is the plasmon resonance frequency. Both σ_0 and τ can be expressed as a function of the carrier density n and mobility μ of graphene, written as $\sigma_0 = ne\mu$ and $\tau = (\pi n)^{1/2}\hbar\mu/ev_F$, where e is elementary charge, and v_F is the Fermi velocity. The relative attenuation is then expressed as $\Delta T = 1 - T(V_g)/T(V_{g,min})$. To fit the attenuation spectra shown in Figure 1, panel c, we take a fixed $\mu = 1300\ cm^2\ V^{-1}\ s^{-1}$ and set n and ω_p as fitting parameters. To plot the polarization-dependent attenuation through the device shown in Figure 2, panel a and Figure 4, panel a, we first calculate the effective average electric field seen by graphene, which is estimated as electric field of the incident beam corrected by the extinction factor $(f(\omega, \theta))^{1/2}$ of the metal grating. $f(\omega, \theta)$ is defined as $f(\omega, \theta) = \cos^2(\theta) + \sin^2(\theta) \times \Phi(\omega)$, where $\Phi(\omega) \in [0, 1]$ is the ratio of the measured transmission at $\theta = 90°$ and 0° when the device is at the charge neutral point. The polarization-dependent

DOI: 10.1021/acs.nanolett.5b00137
Nano Lett. 2015, 15, 4295−4302

attenuation can be then described as $\Delta T = [1 - (T_{high}/T_{low})] \times f(\omega, \theta)$, where T_{high} and T_{low} contribute to the measured transmission in highly and low (charge neutral point) doped graphene. When modeling the spectra, we project the effective electric field (the electric field of the incident light corrected by the factor $f(\omega, \theta)$) to the axes parallel and perpendicular to graphene ribbons. The parallel and perpendicular components contribute to a Drude and plasmonic absorption, respectively. Considering the perturbation of metal electrodes, we assume that the plasmon mode does not extend over the full length of the strip. We estimate that it covers ~80% of the area of the strip. The transmission of the graphene ribbons is described by the same thin-film expression as explained before. In this device, μ is taken to be 800 $cm^2\ V^{-1}\ s^{-1}$, and n is 1.6×10^{13} cm^{-2}. The standing wave plasmon frequency ω_p is given by eq 3.

The photoresponse is calculated based on a photothermoelectric model.[10] The electron temperature rise of each graphene ribbon element from the absorbed THz radiation is determined by the thermal conductance. Since metal contacts stay at room temperature, a temperature profile across the ribbon is generated. The thermoelectric voltage is calculated as[38] $V = \int dx S \times \nabla T$, where ∇T is the electron temperature gradient, and $S(x)$ is the Seebeck coefficient of graphene. The asymmetric metal contacts produce a net thermoelectric signal via (1) nonuniformity in $S(x)$ across the device due to chemical potential pinning[44] at the graphene−metal interface and (2) asymmetric temperature profile due to different contact resistance;[10,45] see ref 10 for additional details. By comparing our device here with the device shown in ref 10, which is bimetal contacted exfoliated graphene on SiO_2 substrate, we assume the same value for metal work functions and a different value for contact resistance. The observed photoresponse is best described by an additional contact resistance R_c = 35 Ω at the region from the gold contact extending 130 nm inside the graphene (the corresponding extra contact resistivity ρ_c = 300 Ω), somewhat less than was found for exfoliated graphene devices on SiO_2 substrates.[10]

■ ASSOCIATED CONTENT

Supporting Information

Movie showing the charge density oscillation in graphene ribbons at the plasmon resonance frequency. This material is available free of charge via the Internet at http://pubs.acs.org.

■ AUTHOR INFORMATION

Corresponding Author

*E-mail: hdrew@physics.umd.edu.

Author Contributions

X.C., A.B.S., T.E.M., H.D.D., and M.S.F. conceived the experiments. X.C. fabricated the devices. X.C. and A.B.S. carried out the FTIR and photoresponse measurements. X.C. did the modeling of the absorption and the photoresponse. M.M.J. did the finite element frequency-domain simulation of the charge density oscillation. L.O.N., R.L.M.-W. and D.K.G. synthesized the graphene on SiC. All authors contributed to the manuscript.

Notes

The authors declare no competing financial interest.

■ ACKNOWLEDGMENTS

This work was sponsored by the U.S. Office of Naval Research (award numbers N000140911064, N000141310712, N000141310865), the National Science Foundation (ECCS 1309750), and IARPA. M.S.F. was supported in part by an ARC Laureate Fellowship.

■ REFERENCES

(1) Bonaccorso, F.; Sun, Z.; Hasan, T.; Ferrari, A. C. *Nat. Photonics* **2010**, *4* (9), 611−622.
(2) Grigorenko, A. N.; Polini, M.; Novoselov, K. S. *Nat. Photonics* **2012**, *6* (11), 749−758.
(3) Mak, K. F.; Ju, L.; Wang, F.; Heinz, T. F. *Solid State Commun.* **2012**, *152* (15), 1341−1349.
(4) Liu, M.; Yin, X.; Ulin-Avila, E.; Geng, B.; Zentgraf, T.; Ju, L.; Wang, F.; Zhang, X. *Nature* **2011**, *474* (7349), 64−67.
(5) Echtermeyer, T. J.; Britnell, L.; Jasnos, P. K.; Lombardo, A.; Gorbachev, R. V.; Grigorenko, A. N.; Geim, A. K.; Ferrari, A. C.; Novoselov, K. S. *Nat. Commun.* **2011**, *2*, 458.
(6) Fei, Z.; Andreev, G. O.; Bao, W.; Zhang, L. M.; S. McLeod, A.; Wang, C.; Stewart, M. K.; Zhao, Z.; Dominguez, G.; Thiemens, M.; Fogler, M. M.; Tauber, M. J.; Castro-Neto, A. H.; Lau, C. N.; Keilmann, F.; Basov, D. N. *Nano Lett.* **2011**, *11* (11), 4701−4705.
(7) Ju, L.; Geng, B.; Horng, J.; Girit, C.; Martin, M.; Hao, Z.; Bechtel, H. A.; Liang, X.; Zettl, A.; Shen, Y. R.; Wang, F. *Nat. Nanotechnol.* **2011**, *6* (10), 630−634.
(8) Strait, J. H.; Nene, P.; Chan, W.-M.; Manolatou, C.; Tiwari, S.; Rana, F.; Kevek, J. W.; McEuen, P. L. *Phys. Rev. B* **2013**, *87* (24), 241410.
(9) Schmadel, D.; Jenkins, G. S.; Drew, H. D. *arXiv: 1311.1605* **2013**.
(10) Cai, X.; Sushkov, A. B.; Suess, R. J.; Jadidi, M. M.; Jenkins, G. S.; Nyakiti, L. O.; Myers-Ward, R. L.; Li, S.; Yan, J.; Gaskill, D. K.; Murphy, T. E.; Drew, H. D.; Fuhrer, M. S. *Nat. Nanotechnol.* **2014**, *9* (10), 814−819.
(11) Mittendorff, M.; Winnerl, S.; Kamann, J.; Eroms, J.; Weiss, D.; Schneider, H.; Helm, M. *Appl. Phys. Lett.* **2013**, *103*, 021113.
(12) Spirito, D.; Coquillat, D.; De Bonis, S. L.; Lombardo, A.; Bruna, M.; Ferrari, A. C.; Pellegrini, V.; Tredicucci, A.; Knap, W.; Vitiello, M. S. *Appl. Phys. Lett.* **2014**, *104*, 061111.
(13) Breusing, M.; Ropers, C.; Elsaesser, T. *Phys. Rev. Lett.* **2009**, *102* (8), 086809.
(14) Winzer, T.; Knorr, A.; Malic, E. *Nano Lett.* **2010**, *10* (12), 4839−4843.
(15) Graham, M. W.; Shi, S.-F.; Ralph, D. C.; Park, J.; McEuen, P. L. *Nat. Phys.* **2013**, *9* (2), 103−108.
(16) Sun, D.; Aivazian, G.; Jones, A. M.; Ross, J. S.; Yao, W.; Cobden, D.; Xu, X. *Nat. Nanotechnol.* **2012**, *7* (2), 114−118.
(17) Kim, M. H.; Yan, J.; Suess, R. J.; Murphy, T. E.; Fuhrer, M. S.; Drew, H. D. *Phys. Rev. Lett.* **2013**, *110* (24), 247402.
(18) Yan, J.; Kim, M. H.; Elle, J. A.; Sushkov, A. B.; Jenkins, G. S.; Milchberg, H. M.; Fuhrer, M. S.; Drew, H. D. *Nat. Nanotechnol.* **2012**, *7* (7), 472−478.
(19) Mak, K. F.; Sfeir, M. Y.; Wu, Y.; Lui, C. H.; Misewich, J. A.; Heinz, T. F. *Phys. Rev. Lett.* **2008**, *101* (19), 196405.
(20) Nair, R. R.; Blake, P.; Grigorenko, A. N.; Novoselov, K. S.; Booth, T. J.; Stauber, T.; Peres, N. M. R.; Geim, A. K. *Science* **2008**, *320* (5881), 1308−1308.
(21) Li, Z. Q.; Henriksen, E. A.; Jiang, Z.; Hao, Z.; Martin, M. C.; Kim, P.; Stormer, H. L.; Basov, D. N. *Nat. Phys.* **2008**, *4* (7), 532−535.
(22) Peres, N. M. R.; Stauber, T.; Castro Neto, A. H. *Europhys. Lett.* **2008**, *84* (3), 38002.
(23) Konstantatos, G.; Badioli, M.; Gaudreau, L.; Osmond, J.; Bernechea, M.; de Arquer, F. P. G.; Gatti, F.; Koppens, F. H. L. *Nat. Nanotechnol.* **2012**, *7* (6), 363−368.
(24) Furchi, M.; Urich, A.; Pospischil, A.; Lilley, G.; Unterrainer, K.; Detz, H.; Klang, P.; Andrews, A. M.; Schrenk, W.; Strasser, G.; Mueller, T. *Nano Lett.* **2012**, *12* (6), 2773−2777.

DOI: 10.1021/acs.nanolett.5b00137
Nano Lett. 2015, 15, 4295−4302

(25) Vicarelli, L.; Vitiello, M. S.; Coquillat, D.; Lombardo, A.; Ferrari, A. C.; Knap, W.; Polini, M.; Pellegrini, V.; Tredicucci, A. *Nat. Mater.* **2012**, *11* (10), 865−871.
(26) Hwang, E. H.; Das Sarma, S. *Phys. Rev. B* **2007**, *75* (20), 205418.
(27) Rana, F. *IEEE Trans. Nanotechnol.* **2008**, *7* (1), 91−99.
(28) Mikhailov, S. A.; Savostianova, N. A. *Phys. Rev. B* **2006**, *74* (4), 045325.
(29) Satou, A.; Ryzhii, V.; Chaplik, A. *J. Appl. Phys.* **2005**, *98*, 034502.
(30) Fei, Z.; Rodin, A. S.; Andreev, G. O.; Bao, W.; McLeod, A. S.; Wagner, M.; Zhang, L. M.; Zhao, Z.; Thiemens, M.; Dominguez, G.; Fogler, M. M.; Neto, A. H. C.; Lau, C. N.; Keilmann, F.; Basov, D. N. *Nature* **2012**, *487* (7405), 82−85.
(31) Yan, H.; Li, X.; Chandra, B.; Tulevski, G.; Wu, Y.; Freitag, M.; Zhu, W.; Avouris, P.; Xia, F. *Nat. Nanotechnol.* **2012**, *7* (5), 330−334.
(32) Basov, D. N.; Fogler, M. M.; Lanzara, A.; Wang, F.; Zhang, Y. *Rev. Mod. Phys.* **2014**, *86* (3), 959−994.
(33) Nikitin, A. Y.; Low, T.; Martin-Moreno, L. *Phys. Rev. B* **2014**, *90* (4), 041407.
(34) Ma, Q.; Gabor, N. M.; Andersen, T. I.; Nair, N. L.; Watanabe, K.; Taniguchi, T.; Jarillo-Herrero, P. *Phys. Rev. Lett.* **2014**, *112* (24), 247401.
(35) Freitag, M.; Low, T.; Xia, F.; Avouris, P. *Nat. Photonics* **2013**, *7* (1), 53−59.
(36) Gabor, N. M.; Song, J. C. W.; Ma, Q.; Nair, N. L.; Taychatanapat, T.; Watanabe, K.; Taniguchi, T.; Levitov, L. S.; Jarillo-Herrero, P. *Science* **2011**, *334* (6056), 648−652.
(37) Song, J. C. W.; Rudner, M. S.; Marcus, C. M.; Levitov, L. S. *Nano Lett.* **2011**, *11* (11), 4688−4692.
(38) Wei, P.; Bao, W.; Pu, Y.; Lau, C. N.; Shi, J. *Phys. Rev. Lett.* **2009**, *102* (16), 166808.
(39) Zuev, Y. M.; Chang, W.; Kim, P. *Phys. Rev. Lett.* **2009**, *102* (9), 096807.
(40) Freitag, M.; Low, T.; Zhu, W.; Yan, H.; Xia, F.; Avouris, P. *Nat. Commun.* **2013**, *4*, 1951.
(41) Nyakiti, L. O.; Wheeler, V. D.; Garces, N. Y.; Myers-Ward, R. L.; Eddy, C. R. J.; Gaskill, D. K. *MRS Bull.* **2012**, *37* (12), 1149−1157.
(42) Niemeyer, J.; Kose, V. *Appl. Phys. Lett.* **1976**, *29* (6), 380−382.
(43) Wu, S.; Kaplan, S. G.; Lihn, H. T. S.; Drew, H. D.; Hou, S. Y.; Phillips, J. M.; Barbour, J. C.; Venturini, E. L.; Li, Q.; Fenner, D. B. *Phys. Rev. B* **1996**, *54* (18), 13343−13347.
(44) Huard, B.; Stander, N.; Sulpizio, J. A.; Goldhaber-Gordon, D. *Phys. Rev. B* **2008**, *78* (12), 121402.
(45) Khomyakov, P. A.; Starikov, A. A.; Brocks, G.; Kelly, P. J. *Phys. Rev. B* **2010**, *82* (11), 115437.

DOI: 10.1021/acs.nanolett.5b00137
Nano Lett. 2015, 15, 4295−4302